

Spike Imaging Velocimetry: Dense Motion Estimation of Fluids Using Spike Cameras

Yunzhong Zhang¹, Bo Xiong², You Zhou¹, Changqing Su², Zhen Cheng³, Zhaofei Yu², Xun Cao¹ and Tiejun Huang²

¹Nanjing University

²Peking University

³Tsinghua University

ltq@smail.nju.edu.cn, boxiong11@outlook.com, zhouyou@nju.edu.cn, qing1286765276@gmail.com, zcheng@mail.tsinghua.edu.cn, yuzf12@pku.edu.cn, caoxun@nju.edu.cn, tjhuang@pku.edu.cn

Abstract

The need for accurate and non-intrusive flow measurement methods has led to the widespread adoption of Particle Image Velocimetry (PIV), a powerful diagnostic tool in fluid motion estimation. This study investigates the tremendous potential of spike cameras (a type of ultra-high-speed, high-dynamic-range camera) in PIV. We propose a deep learning framework, Spike Imaging Velocimetry (SIV), designed specifically for highly turbulent and intricate flow fields. To aggregate motion features from the spike stream while minimizing information loss, we incorporate a Detail-Preserving Hierarchical Transform (DPHT) module. Additionally, we introduce a Graph Encoder (GE) to extract contextual features from highly complex fluid flows. Furthermore, we present a spike-based PIV dataset, Particle Scenes with Spike and Displacement (PSSD), which provides labeled data for three challenging fluid dynamics scenarios. Our proposed method achieves superior performance compared to existing baseline methods on PSSD. The datasets and our implementation of SIV are open-sourced in the supplementary materials.

1 Introduction

The need for accurate and non-intrusive flow measurement methods has led to the widespread adoption of Particle Image Velocimetry (PIV), a powerful diagnostic tool in fluid dynamics research. This technique has been widely applied to critical topics such as studying the aerodynamic shapes of aircraft[Kompenhans *et al.*, 2000], optimizing vehicle designs to reduce air resistance[Nakagawa *et al.*, 2016], improving energy conversion efficiency in combustion processes[Chen *et al.*, 2022], understanding the impact of blood flow dynamics on diseases[Raschi *et al.*, 2012], and predicting the spread of water pollution[MoayeriKashani *et al.*, 2016].

In PIV experiments or simulations, tracer particles(e.g., silver-coated particles) are introduced into the fluid to scatter optical signals. By estimating their displacements, PIV

can infer the velocities of the fluid in which they are suspended. The success of optical flow networks[Dosovitskiy

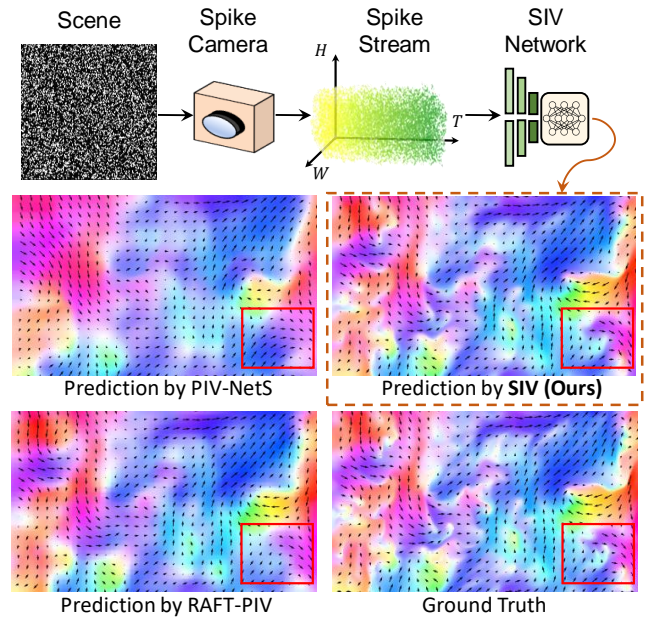


Figure 1: A schematic of fluid velocity field estimation based on spike cameras, and a comparison of the complex velocity field estimated using our proposed SIV network with PIV-NetS[Cai *et al.*, 2019b] and RAFT-PIV[Lagemann *et al.*, 2021].

et al., 2015; Sun *et al.*, 2018; Teed and Deng, 2020] inspires the development of learning-based PIV algorithms[Cai *et al.*, 2019b; Cai *et al.*, 2019a; Lagemann *et al.*, 2021]. However, the performance improvements of these PIV networks mainly rely on advancements in optical flow estimation networks, rather than targeted improvements that incorporate the specific characteristics of the flow field. Although optical flow networks generally exhibit good generalization ability, the characteristics of fluid scenes cannot be ignored for further performance improvement. Turbulence is an irregular flow phenomenon occurring at high Reynolds numbers. When measuring the turbulent velocity field with PIV, this scenario is significantly different from macroscopic worlds, with the

following key challenges:

- (1) The fluid often moves rapidly within the field of view.
- (2) Signals are only present in regions with tracer particles, and since the particle volume is small, downsampling may lead to signal loss;
- (3) Unlike solids, the fluid is highly unstructured overall, despite the presence of vortices of different scales (called quasi-order structures).

These challenges often coexist in turbulence. Challenge (1) places high demands on experimental hardware, typically requiring ultra-high-speed cameras. Challenge (2) requires us to carefully address potential resolution loss in the network. Challenge (3) introduces problems to the extraction of context features. Based on these characteristics, we propose improvements in both hardware and algorithm aspects.

In terms of hardware, we explore the application of spike cameras (a type of neuromorphic camera) for PIV. We argue that using spike cameras instead of CMOS sensors in fluid measurement tasks offers several advantages:

High temporal resolution (HTR). Spike cameras can achieve ultra-high temporal resolution (20000Hz), reducing the interval Δt between the source and target time, and providing rich temporal information for accurate predictions. This allows the spike camera to cope well with Challenge (1); **High dynamic range (HDR).** When particles accumulate in large numbers, local regions may become overly bright, exceeding the dynamic range of conventional cameras. Spike cameras asynchronously accumulate photons at each pixel, inherently possessing a much larger dynamic range compared to CMOS sensors. This makes them more advantageous in scenarios with uneven brightness (such as inappropriate lighting or particles moving toward concentrated areas);

Reduced experimental complexity. Spike cameras can continuously capture images at high frame rates with exceptionally low bandwidth and eliminate the need for synchronization controllers to modulate the camera and laser.

In terms of algorithm, we introduce a specialized network, Spike Imaging Velocimetry (SIV) to estimate fluid displacement fields. We propose two modules, the Detail-Preserving Hierarchical Transform (DPHT) designed in consideration of Challenge (2), and the Graph Encoder (GE) mainly designed for Challenge (3). We also introduce a dataset called Particle Scenes with Spike and Displacement (PSSD). PSSD comprises labeled data addressing three common motion estimation scenarios: steady turbulence (Problem 1), high-speed flow (Problem 2), and high dynamic range scenarios (Problem 3). In the experimental section, we conduct comparative analyses of our method against both image-based and spike-based approaches. Our proposed SIV achieves state-of-the-art performance across all three sub-datasets. The effectiveness of the proposed modules is further demonstrated through ablation studies. The main contributions of this work are as follows:

1. Explore a feasible approach for applying spike cameras to fluid velocity measurement;
2. From the perspective of fluid dynamics, especially turbulent flows, and the characteristics of the PIV scenarios, design a suitable network structure SIV, including two new modules: DPHT and GE;

3. Propose a PIV dataset for recording continuous fluid motion with spike cameras, which includes four flow types and three challenging experimental scenarios.

2 Related Work

2.1 Spike-based Optical Flow Estimation

The spike camera [Dong *et al.*, 2021; Huang, 2019] is a type of neuromorphic camera (NeurCam). Inspired by biological visual neural structures and mechanisms, NeurCams emulate the encoding principles of the primate retina. Spike cameras mimic the encoding principles of the central fovea in the retina, providing continuous visual information with ultra-high temporal resolutions, high dynamic range (HDR), and significantly reduced energy consumption and latency, making them well-suited for high-speed motion scenarios. Their pixels independently accumulate photons and emit a spike when the accumulated intensity exceeds a certain threshold. This process maps the incoming photon stream into the spike stream, which preserves spatiotemporal relationships and can be reconstructed into images. For a detailed explanation of the working mechanism, refer to [Dong *et al.*, 2021]. The application of spike cameras in optical flow estimation provides significant insights for this study. Although optical flow estimation is generally used to estimate the motion of macroscopic objects, its principles and objectives are aligned with those of Particle Image Velocimetry (PIV). The techniques employed in PIV for image registration and displacement estimation are essentially a variant of optical flow estimation. Spike-based optical flow estimation is still a relatively new field. [Hu *et al.*, 2022] introduced a specialized neural network architecture for spike-based optical flow estimation. This structure can adaptively eliminate motion blur in spike streams based on prior motion information. A framework based on [Teed and Deng, 2020] is proposed by [Zhao *et al.*, 2022] to handle continuous spike streams and is then extended by [Zhao *et al.*, 2024] to suppress the adverse effects of randomness in spike streams. [Chen *et al.*, 2023] proposed a self-supervised approach to learn optical flow from spike cameras, which is then extended by [Xia *et al.*, 2024].

2.2 Image-based PIV Algorithms

Many traditional image-based PIV algorithms [Lourenco and Krothapalli, 1995; Nobach and Honkanen, 2005] usually involve applying a fast Fourier transform (FFT) between two subregions of image pairs, known as interrogation areas (IA). Displacement is then determined by finding the maximum correlation between the two interrogation windows, which is similar to the correlation method in optical flow estimation to some extent. However, traditional methods depend on finely tuned parameters and complex optimization techniques. With advancements in optical flow networks, various architectures [Dosovitskiy *et al.*, 2015; Sun *et al.*, 2018; Teed and Deng, 2020] are developed to predict dense displacement fields of macroscopic objects with high accuracy. Early PIV networks like PIV-DCNN [Lee *et al.*, 2017] laid the groundwork for these developments. PIV-NetS [Cai *et al.*, 2019b] is capable of generating full-resolution displacement outputs. [Cai *et al.*, 2019a] adapt LiteFlowNet [Hui *et al.*,

2018] to PIV. RAFT-PIV[Lagemann *et al.*, 2021], derived from RAFT[Teed and Deng, 2020], has shown exceptional performance on multiple datasets. Additionally, unsupervised learning frameworks for PIV[Zhang and Piggott, 2020; Zhang *et al.*, 2023a] have been introduced, reducing reliance on the extremely difficult-to-obtain ground-truth displacements. Other recent PIV networks include LIMA[Manickathan *et al.*, 2023], CC-FCN[Gao *et al.*, 2021], En-FlowNetC[Ji *et al.*, 2024a], ARAFT-FlowNet[Han and Wang, 2023], OFVNetS[Ji *et al.*, 2024b], and PIV-PWCNet[Zhang *et al.*, 2023b]. However, the performance improvements of these PIV networks mainly rely on advancements in optical flow estimation networks, rather than targeted improvements that incorporate the specific characteristics of the flow field, and most of them have not been open-sourced.

2.3 Event-based PIV Algorithms

The event camera(such as DVS[Lichtsteiner *et al.*, 2008], DAVIS[Moeys *et al.*, 2017], ATIS[Posch *et al.*, 2010], CeleX[Huang *et al.*, 2017]) is another type of NeurCam, which is inspired by the peripheral retina[Rebecq *et al.*, 2019]. Unlike spike cameras, event cameras independently monitor the change in light intensity (increase or decrease) at each pixel and generate signals based on the local pixel information of dynamic changes. When the brightness change of a pixel exceeds a preset threshold, the camera records this change event (brightness increase as a positive event, brightness decrease as a negative event) and outputs its timestamp, position, and change value as data. However, due to the lack of absolute intensity values, event cameras struggle to reconstruct complete images, particularly in static regions and with fine textures. The application of event cameras to PIV has already been explored by [Willert and Kliner, 2022] and [Willert, 2023]. Similar to the spike camera, the event camera offers higher temporal resolution, high dynamic range, low latency, and reduced experimental complexity. However, event cameras are only sensitive to objects with obvious motion and have hardly any output signal in stationary regions. This can be a weakness compared to spike cameras, considering that not all areas of the flow field may be moving at high speed.

3 Preliminary

3.1 The Working Principle of the Spike Camera

Each photosensitive element in a spike camera generates spike streams sequentially over time. A "1" in the stream indicates that a spike has occurred (i.e., the threshold has been reached), while a "0" indicates an ongoing accumulation state. The Integral-and-Fire (IF) mechanism of spike cameras can be mathematically represented as follows:

$$A(\mathbf{x}, t) = \int_0^t \alpha \cdot I(\mathbf{x}, \tau) \bmod \theta, \quad (1)$$

Where $A(\mathbf{x}, t)$ represents the voltage of the accumulator at pixel $\mathbf{x} = (x, y)$ at time τ , and θ is the threshold of the comparator. The spike camera's output is a spatiotemporal binary stream S of size $H \times W \times N$, where H and W are the height and width of the sensor, respectively, and N represent

the time length of the spike stream. Compared to traditional cameras, spike cameras preserve richer visual information regarding both temporal resolution and brightness representation.

3.2 Data Generation

Our proposed dataset, Particle Scenes with Spike and Displacement (PSSD), includes three sub-datasets: Steady Turbulence (Problem 1), High-speed Flow (Problem 2), and HDR Scenes (Problem 3). Each sub-dataset comprises 10,000 sample sequences of spike streams and the corresponding ground truth turbulent displacement fields when $\Delta t = 21$ (about 1.05 ms) and $\Delta t = 11$ (about 0.55 ms). Additionally, we provide corresponding pairs of images for comparative analysis for image-based methods. We use the reference flow field to simulate the motion of the scene and construct a virtual spike camera to trigger the spike stream. The reference flow field data are taken from the high-precision numerical simulation database used for turbulence research, Johns Hopkins Turbulence Database (JHTDB)[Li *et al.*, 2008]. JHTDB employs Direct Numerical Simulation (DNS) to simulate turbulent flow fields. DNS directly solves the Navier-Stokes equations without any model assumptions or simplifications, enabling precise capture of all scales in turbulent flow. This method resolves the fluid motion in both space and time with high-resolution grids, accurately capturing the complex and multi-scale nature of turbulence. Additional details about the dataset can be found in our supplementary materials.

4 Approaches

4.1 Overall Architecture

Problem definition. Let $\mathbf{S} \in \mathbb{B}^{H \times W \times T}$ represent the spike stream recorded by the spike camera. \mathbb{B} is the binary domain. We aim to estimate the displacement \mathbf{D} of particles in the fluid between time moments t and $t + \Delta t$. At the pixel level, for any given pixel $\mathbf{p} = (x, y)$ at t , we need to find a unique correspondence formulated by:

$$\mathcal{I}(\mathbf{p}, t) \leftarrow \mathcal{I}(\mathbf{p}, t + \Delta t). \quad (2)$$

Here, \mathcal{I} is the mapping of the spike stream \mathbf{S} in the high-dimensional feature space, representing the scene information, i.e., $\mathcal{I} = \text{Rep}(\mathbf{S})$.

Network architecture. The primary structure of the SIV network is shown in Figure 2. To represent the scenes at moments t and $t + \Delta t$, we extract spike stream segments (source and target) near these two moments, denoted as \mathbf{S}_s and \mathbf{S}_t , and input them into the network. Firstly, through the proposed DPHT module, the sub-stream \mathbf{S}_s and \mathbf{S}_t are embedded into the representations \mathbf{R}_s and \mathbf{R}_t by our proposed DPHT module. Motion features $\mathbf{F}_{s,m}$ and $\mathbf{F}_{t,m}$ are extracted from \mathbf{R}_s and \mathbf{R}_t . Through the proposed Graph Encoder, the context feature \mathbf{F}_c is extracted from \mathbf{R}_t . Subsequently, the enhanced features $\mathbf{F}_{s,m}$, $\mathbf{F}_{t,m}$ and \mathbf{F}_c undergo an iterative optimization process in a pyramid structure, ranging from coarse (1/16 downsampled branch) to fine (1/4 downsampled branch). In each branch, similar to DIP[Zheng *et al.*, 2022],

the Inverse Patchmatch Block is used to construct the correlation volume, and is aggregated through a GRU. Finally, the Local Search Block estimates the residual displacement field ΔD by searching for local cost based on the current displacement field estimate, and cost aggregation is performed through another GRU.

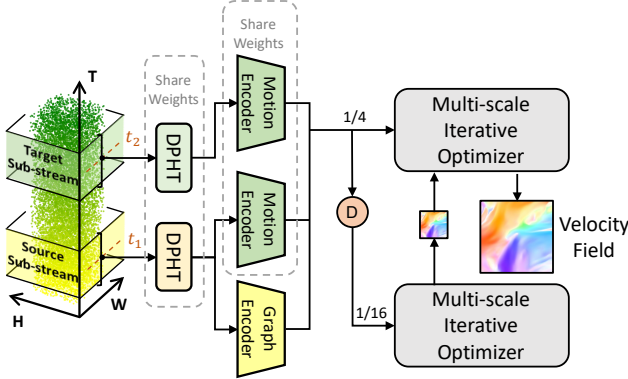


Figure 2: The overall network structure of SIV includes motion feature extraction supported by DPHT and the motion encoder, context feature extraction supported by DPHT and the Graph Encoder, along with a multi-scale iterative optimization process.

4.2 Detail-Preserving Hierarchical Transform

[Zhao *et al.*, 2024] demonstrates that using a multi-layer hierarchical structure to characterize spike streams can effectively suppress the influence of randomness in spikes and enhance the feature extraction capability of the network. Low-level features mainly focus on local details, while high-level features aggregate these low-level features to express more complex meanings. However, our ablation experiments (see Table 2) show that directly using multi-level representations does not achieve optimal performance improvement for PIV. This is because, as mentioned in the Introduction, the reduction in resolution or scale of feature maps leads to a significant loss of detail information. Furthermore, these details may not be critical for macroscopic objects, but considering that the particles in PIV are small and the fluid motion is highly intricate and complex, even the loss of detail information could result in an increase in local prediction errors. Moreover, the sparse and dark regions without particles essentially carry little to no signal, much of the information in a small region may stem from the bright particles. Based on these considerations, we designed a 3D Detail-Preserving Downsampling unit in which a bunch of 3D convolutions and 3D max poolings are incorporated (as shown in Figure 3(a)) to reduce the progressive loss of important information across the multi-layer structure while enabling the network to aggregate features at multiple scales. We refer to the entire block in Figure 3(a) as the Detail-Preserving Hierarchical Transform (DPHT).

3D Detail-Preserving downsampling. As shown in Figure 3(a), suppose the input of level l is a feature vector $\mathbf{x}^{(l)}$, and the processing of $\mathbf{x}^{(l)}$ at this level is as follows:

$$\mathbf{x}_{\text{out}}^{(l)} = \mathcal{D}^{(l)}(\mathbf{x}^{(l)}) = \mathcal{F}_{2C}(\mathcal{F}_{3C}(\mathbf{x}^{(l)}) + \mathcal{F}_{3\text{MP}}(\mathbf{x}^{(l)})), \quad (3)$$

Here, \mathcal{F}_{3C} represents a $5 \times 3 \times 3$ 3D convolution, $\mathcal{F}_{3\text{MP}}$ is a combination of a 3D max pooling operation and a $5 \times 1 \times 1$ 3D convolution, and \mathcal{F}_{2C} refers to a sequential stack of 2D convolutions. The output of the previous level serves as the input to the next level, i.e., $\mathbf{x}^{(l+1)} = \mathbf{x}_{\text{out}}^{(l)} = \mathcal{D}^{(l)}(\mathbf{x}^{(l)})$.

Global temporal aggregation. In this step, the output feature vectors from each level are further refined by several convolutions (for detailed information, refer to the supplementary materials), and then concatenated together to form the final representation of the DPHT:

$$\mathbf{R} = \mathcal{A}_m[\mathbf{x}_{\text{out}}^{(l=1)} \oplus \mathbf{x}_{\text{out}}^{(l=2)} \oplus \mathbf{x}_{\text{out}}^{(l=3)}], \quad (4)$$

\oplus represents concatenation, and \mathcal{A}_m denotes convolution. As shown in Figure 3, we use DPHT as a pre-representation method before motion feature extraction and context information extraction, obtaining \mathbf{R}_s and \mathbf{R}_t for source sub-stream and target sub-stream, respectively.

4.3 Graph Encoder

Turbulent motion is highly complex, and extracting context information from turbulence is challenging. Therefore, [Yu *et al.*, 2021] argued that context extractors are unnecessary for PIV and removed this structure from their network. However, we hold a different view: despite the spatially chaotic nature of turbulence, there still exist multi-scale vortex structures (referred to as quasi-order structures), making the extraction of context information meaningful. To achieve this, we introduce Graph Convolutional Unit (GCU) in the context extractor, referring to the entire context extractor as the Graph Encoder. Graph convolutions weight the relationships between nodes using an adjacency matrix, performing local aggregation. Each node not only focuses on its own features but also passes information from neighboring nodes (as defined by the adjacency matrix) to itself. We believe that this approach is particularly suited for capturing spatial or topological structures in the PIV data, especially when the quasi-order structures of the flow is highly complex topologically. This situation arises particularly in cases with extremely high flow speeds (meaning high Reynolds numbers). When the Reynolds number is sufficiently high, turbulence experiences a cascade process from large-scale vortices to small-scale vortices (Kolmogorov scale) [Kolmogorov, 1991]. This cascade process is the transfer of energy from large vortices to small vortices in turbulence, with each vortex disturbing the surrounding flow field, further complicating the flow.

Graph projection. The first step is to map the preliminary context information $\mathbf{R}_c = \mathbf{R}_s$ extracted from DPHT from the general coordinate space to the graph space. The projection operation decouples the position information from the original grid features, making the resulting low-dimensional node feature representations more compact and expressive. The mapped context node representations, denoted as $\mathbf{V}_c = \{v_c^1, \dots, v_c^n\}$, contain appearance features related to the shape and regional information of the scene context. Given \mathbf{R}_c , we can use the projection function $\mathcal{P}_{R \rightarrow V}(\cdot)$ to assign features with similar representations to the same node, resulting $\mathbf{V}_c \in \mathbb{R}^{C \times K}$, where C indicates channel number and K is a hyper-parameter representing the number of nodes. Since

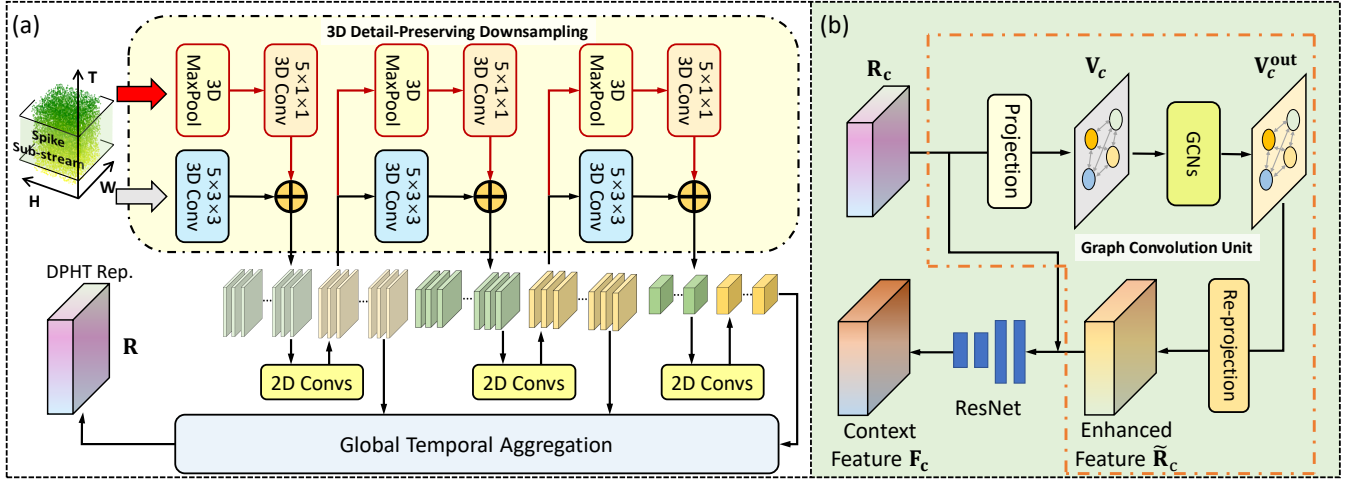


Figure 3: (a) A demonstration of the Detail-Preserving Hierarchical Transform (DPHT) module. (b) A brief illustration of Graph Encoder (GE) module.

$\mathcal{P}_{R \rightarrow V}(\cdot)$ we define is a linear combination of feature vectors within the grid space, i.e., $\mathbf{V}_c = \mathcal{P}_{R \rightarrow V}(\mathbf{R}_c)$, the resulting nodes can theoretically aggregate both long-range and short-range information across the entire feature map, which could be beneficial for turbulent scenes with multi-scale quasi-order structures. This is formulated by,

$$v_{c,i} = \mathcal{N}\left(\sum_{\forall j} z_{ij} \cdot \mathbf{R}_{c,j}\right). \quad (5)$$

Here, $\mathcal{N}(\cdot)$ is the L_2 -normalization function applied to the channel dimension of each node vector, and z_{ij} denotes the projection weights computed by a CNN, i.e., $z = \mathcal{P}_{R \rightarrow V}(\mathbf{R}_c) \in \mathbb{R}^{(H \times W) \times K}$.

Graph convolution. After obtaining the nodes \mathbf{v}_c in the graph space, the adjacency matrix $\mathbf{A} = \mathbf{V}_c^T \mathbf{V}_c$ can be derived by calculating the similarity between all node vectors. We utilize the graph convolution \mathcal{G} from [Selvan *et al.*, 2020] to further propagate information across the graph. Specifically, for a single graph convolution with its parameter W_g , the operation is defined as

$$\mathbf{V}'_c = \mathcal{G}(\mathbf{V}_c, \mathbf{A}) = \sigma(\mathbf{A} \mathbf{V}_c^T W_g), \quad (6)$$

where $\sigma(\cdot)$ is a non-linear activation function. Two serial graph convolutional networks (GCNs) are used to capture the relationships between nodes. The node features updated by the GCNs are given by

$$\mathbf{V}_c^{\text{out}} = \mathcal{G}_2[\mathcal{G}_1(\mathbf{V}_c, \mathbf{A}), \mathbf{A}], \quad (7)$$

Graph re-projection. Our graph re-projection operation $\mathcal{P}_{V \rightarrow R}(\cdot)$ takes the transformed vertex features $\mathbf{V}_c^{\text{out}}$ and the projection weight matrix $\mathbf{Z} = [z_{ij}]$ as inputs, generating a 2D feature map $\tilde{\mathbf{R}}_c$. Since inverting the projection weight matrix is not feasible, we follow the approach in [Li and Gupta, 2018; Luo *et al.*, 2022] and compute the enhanced grid context features $\tilde{\mathbf{R}}_c$ by re-weighting the vertex features $\mathbf{V}_c^{\text{out}}$. This is given by,

$$\tilde{\mathbf{R}}_c = \mathcal{P}_{V \rightarrow R}(\mathbf{V}_c^{\text{out}}, \mathbf{Z}) = \mathbf{Z} \mathbf{V}_c^{\text{out}T}. \quad (8)$$

Thus, $\mathcal{P}_{V \rightarrow R}$ thus linearly interpolates 2D pixel features based on the node assignments of the 2D grid features, without additional parameters. Note that even if two pixels are assigned to the same node, they will have different features after re-projection. Therefore, the GCU may preserve the spatial details of the signal. Finally, these projection results can be integrated into an existing residual extractor network \mathcal{R} introduced by [Teed and Deng, 2020]. Final context feature \mathbf{F}_c given by,

$$\mathbf{F}_c = \mathcal{R}(\mathbf{R}_c + \alpha \tilde{\mathbf{R}}_c), \quad (9)$$

where α denotes a learnable parameter that is initialized as 0 and gradually performs a weighted sum.

5 Experimental Results

In this section, we evaluate our method on the PSSD dataset and compare its performance with other traditional and learning-based methods. Additionally, we conduct a series of ablation experiments to assess the effectiveness of the proposed modules.

5.1 Experimental Details

SIV is implemented using the PyTorch framework on a single NVIDIA RTX 2080 Ti GPU. We employ the Adam optimizer with a warm-up strategy during training. The model parameters for DIP are consistent with those specified in the original paper [Zheng *et al.*, 2022]. For each problem, we train the model for 100 epochs with an initial learning rate of 10^{-4} , applying an 85% decay every 10 epochs. The number of iterative refinements is set to 10, and the batch size is 4.

Following [Cai *et al.*, 2019b] and [Lagemann *et al.*, 2021], we use endpoint error (EPE) as the primary evaluation metric for comparing different algorithms. Additionally, given the absence of a dedicated outlier metric in PIV, we introduced Root Mean Squared Error (RMSE) as a supplementary metric due to its sensitivity to outliers.

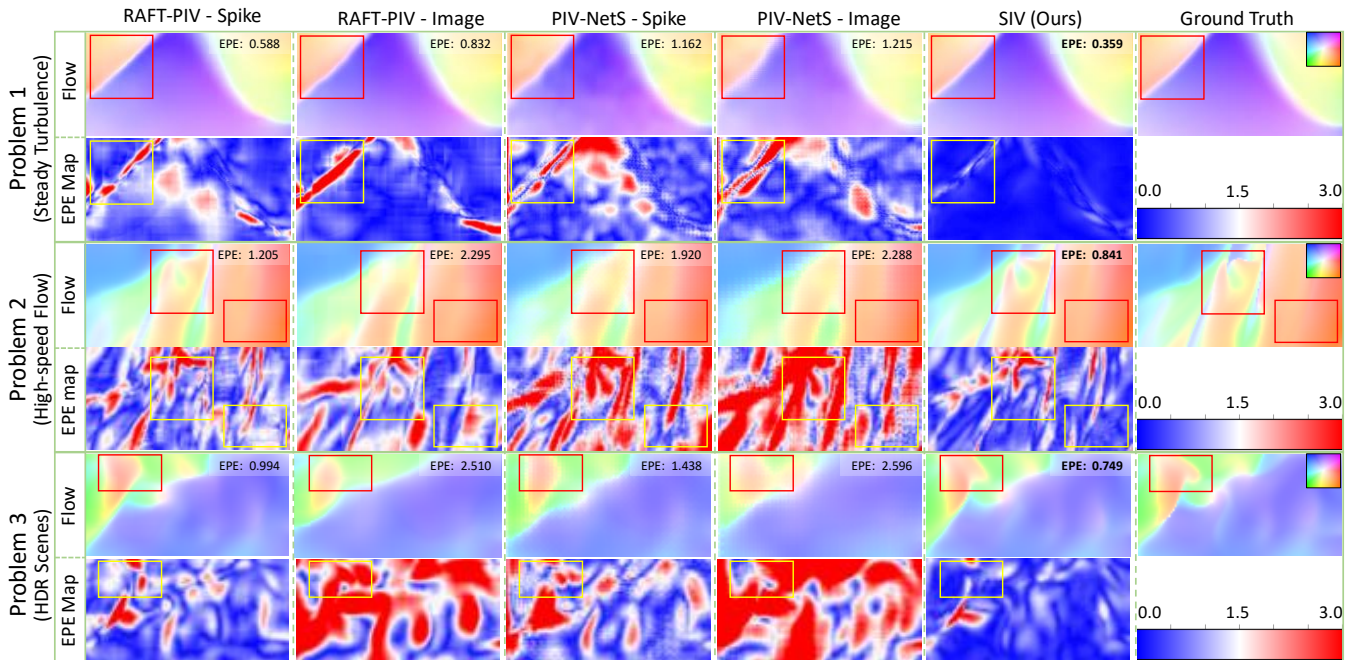


Figure 4: Visualization examples of different algorithms in Steady Turbulence (Problem 1), High-speed Flow (Problem 2), and HDR Scenes (Problem 3) are shown. For each problem, the red box in the top optical flow map and the yellow box in the bottom EPE error map indicate the same region of the flow field.

Since SIV outputs a prediction sequence of length N at each iteration, the loss function is defined as:

$$loss = \sum_{i=0}^{i=N} w_i \cdot \|f_i - f_{gt}\|_1, w_i = \gamma^{N-i-1}. \quad (10)$$

We set $\gamma = 0.8$ during training.

5.2 Comparative Experiments

To evaluate the effectiveness of our proposed method, we conduct extensive experiments on the PSSD dataset. The experiments are performed under identical settings to ensure fairness in the results.

We compare our method with multiple open-source baselines, including a traditional PIV algorithm[Cai *et al.*, 2018], PIV networks (PIV-NetS[Cai *et al.*, 2019b], RAFT-PIV[Lagemann *et al.*, 2021]), as well as their spike versions, and spike-based optical flow networks (SCFlow[Hu *et al.*, 2022], HiST-SFlow[Zhao *et al.*, 2024]).

Results on Problem 1. In the steady flow scenario, the fluid moves at a moderate speed. In both the time intervals of 1 and 2, SIV achieves the smallest EPE and RMSE, providing the optimal estimation. Compared to the suboptimal methods, SIV reduces the EPE by 26.1% when $\Delta t = 21$. The traditional coarse-to-fine HS[Cai *et al.*, 2018] method can only yield relatively reasonable predictions when the time interval and displacement are small, which reflects, to some extent, the challenge of the dataset. Figure 4 shows the displacement field predictions (optical flow maps) and error maps for different methods in PIV. The red boxes in the optical flow map correspond to the yellow boxes in the error map. The

marked region in Problem 1 is a smooth boundary between the two components. By comparing with the ground truth optical flow map, it is clear that the optical flow map shapes predicted by SIV and the spike version of RAFT-PIV[Lagemann *et al.*, 2021] are mostly accurate, while other methods show varying degrees of distortion in this region. In the error map, it is more intuitive to see that the red areas (high error regions) in SIV are much fewer.

Results on Problem 2. Problem 2 represents high-speed scenarios with greater particle displacements. SIV maintains its lead in all test scenarios, with a 23.3% reduction in EPE at $\Delta t = 21$ compared to the suboptimal method. The traditional method struggles to make effective predictions in this scenario. In the visualization example of Problem 2 shown in Figure 4, the marked area includes a fine flow field shaped like a "human hand" and a "laminar flow region" with very high flow speed. The predicted flow field shape of SIV is very close to the ground truth, and the error in the high-speed "laminar flow region" is significantly smaller than that of other methods.

Results on Problem 3. Problem 3 reflects scenarios with uneven lighting, where areas may exist that cause overexposure in traditional cameras (this issue does not occur in spike cameras due to their principle). SIV still achieves the best performance across all sub-datasets. In the visualization example of Problem 3 (see Figure 4), only SIV predicts a flow field in the marked region that is nearly consistent with the ground truth, and has the fewest red areas (high error regions) in the error map. As we anticipated, in Problem 3, spike-based methods outperform image-based methods, reflecting the high dynamic range advantage of spike cameras under uneven light-

Methods	Channel		Isotropic		Mhd		Mixing		Average		
	$\Delta t = 21$	$\Delta t = 11$	$\Delta t = 21$	$\Delta t = 11$	$\Delta t = 21$	$\Delta t = 11$	$\Delta t = 21$	$\Delta t = 11$	$\Delta t = 21$	$\Delta t = 11$	
Problem 1	SIV (ours)	0.242 / 0.284	0.157 / 0.182	0.918 / 1.288	0.574 / 0.765	0.638 / 0.934	0.407 / 0.563	0.700 / 1.076	0.433 / 0.616	0.625 / 0.895	0.393 / 0.532
	RAFT-PIV - Image	0.377 / 0.437	0.215 / 0.249	2.181 / 2.769	1.252 / 1.574	1.336 / 1.701	0.842 / 1.072	1.875 / 2.486	1.064 / 1.394	1.442 / 1.848	0.843 / 1.072
	RAFT-PIV - Spike	0.347 / 0.401	0.208 / 0.240	1.223 / 1.570	0.755 / 0.942	0.857 / 1.136	0.557 / 0.731	0.958 / 1.288	0.581 / 0.755	0.846 / 1.099	0.525 / 0.667
	PIV-NetS - Image	0.545 / 0.904	0.301 / 0.478	2.560 / 3.136	1.497 / 1.819	1.574 / 2.121	0.985 / 1.284	2.247 / 2.845	1.320 / 1.651	1.731 / 2.253	1.026 / 1.308
	PIV-NetS - Spike	0.553 / 0.821	0.289 / 0.424	1.507 / 1.991	0.874 / 1.124	1.252 / 1.782	0.734 / 1.019	1.382 / 1.903	0.782 / 1.040	1.173 / 1.624	0.670 / 0.902
	SCFlow	0.354 / 0.468	0.222 / 0.284	2.232 / 2.706	1.305 / 1.628	1.374 / 1.703	0.901 / 1.110	2.132 / 2.684	1.169 / 1.435	1.522 / 1.890	0.899 / 1.114
	HiST-SFlow	0.369 / 0.424	0.224 / 0.256	1.271 / 1.614	0.796 / 0.980	0.964 / 1.250	0.611 / 0.784	1.029 / 1.354	0.637 / 0.809	0.908 / 1.160	0.567 / 0.708
	coarse-to-fine HS	6.790 / 8.448	0.509 / 0.655	7.415 / 9.354	1.998 / 3.079	7.683 / 10.783	2.558 / 4.463	9.388 / 7.274	1.954 / 3.146	7.819 / 9.751	1.755 / 2.836
Problem 2	SIV (ours)	0.366 / 0.443	0.256 / 0.300	1.721 / 2.602	1.076 / 1.521	1.098 / 1.671	0.717 / 1.026	1.482 / 2.493	0.907 / 1.412	1.167 / 1.802	0.739 / 1.065
	RAFT-PIV - Image	0.665 / 0.785	0.368 / 0.434	4.730 / 5.952	2.635 / 3.297	2.320 / 2.906	1.366 / 1.707	4.305 / 5.572	2.368 / 3.065	3.005 / 3.804	1.684 / 2.126
	RAFT-PIV - Spike	0.688 / 0.792	0.412 / 0.477	2.410 / 3.169	1.483 / 1.882	1.468 / 1.936	0.959 / 1.236	2.071 / 2.864	1.241 / 1.649	1.659 / 2.190	1.024 / 1.311
	PIV-NetS - Image	1.163 / 1.896	0.683 / 1.029	4.866 / 5.944	2.830 / 3.409	2.673 / 3.719	1.643 / 2.207	4.347 / 5.497	2.500 / 3.095	3.262 / 4.264	1.914 / 2.435
	PIV-NetS - Spike	0.887 / 1.552	0.540 / 0.836	3.172 / 4.155	1.818 / 2.315	2.392 / 3.400	1.410 / 1.963	3.067 / 4.154	1.744 / 2.316	2.379 / 3.315	1.378 / 1.857
	SCFlow	0.694 / 0.716	0.403 / 0.486	4.689 / 5.975	2.613 / 3.156	2.387 / 3.055	1.391 / 1.697	4.326 / 5.262	2.380 / 3.123	3.024 / 3.752	1.696 / 2.116
	HiST-SFlow	0.556 / 0.641	0.364 / 0.419	2.212 / 2.947	1.365 / 1.756	1.404 / 1.879	0.998 / 1.308	1.911 / 2.693	1.179 / 1.595	1.521 / 2.040	0.976 / 1.269
	coarse-to-fine HS	20.691 / 20.993	8.244 / 9.628	17.164 / 19.627	8.051 / 9.944	17.469 / 21.594	8.170 / 11.252	17.131 / 19.572	7.936 / 9.970	18.114 / 20.447	8.100 / 10.199
Problem 3	SIV (ours)	0.241 / 0.286	0.155 / 0.181	0.903 / 1.282	0.564 / 0.761	0.621 / 0.916	0.393 / 0.542	0.698 / 1.106	0.437 / 0.634	0.616 / 0.897	0.389 / 0.530
	RAFT-PIV - Image	0.447 / 0.523	0.244 / 0.286	2.694 / 3.334	1.495 / 1.847	1.447 / 1.808	0.888 / 1.104	2.311 / 2.948	1.271 / 1.613	1.725 / 2.153	0.974 / 1.213
	RAFT-PIV - Spike	0.320 / 0.373	0.200 / 0.232	1.203 / 1.558	0.740 / 0.939	0.798 / 1.061	0.530 / 0.698	0.946 / 1.297	0.576 / 0.770	0.817 / 1.072	0.512 / 0.660
	PIV-NetS - Image	0.667 / 0.991	0.343 / 0.513	2.786 / 3.357	1.602 / 1.924	1.641 / 2.164	0.956 / 1.258	2.393 / 2.988	1.378 / 1.709	1.872 / 2.375	1.070 / 1.351
	PIV-NetS - Spike	0.476 / 0.789	0.247 / 0.406	1.420 / 1.914	0.856 / 1.134	1.157 / 1.695	0.716 / 1.021	1.342 / 1.891	0.774 / 1.063	1.099 / 1.572	0.648 / 0.906
	SCFlow	0.462 / 0.743	0.269 / 0.433	1.850 / 2.206	0.837 / 1.008	1.300 / 1.915	0.774 / 1.142	1.972 / 2.618	0.769 / 1.040	1.396 / 1.871	0.662 / 0.905
	HiST-SFlow	0.329 / 0.381	0.180 / 0.210	1.179 / 1.523	0.640 / 0.828	0.832 / 1.093	0.452 / 0.616	0.960 / 1.302	0.476 / 0.663	0.825 / 1.075	0.437 / 0.579
	coarse-to-fine HS	7.908 / 8.946	1.044 / 1.648	7.924 / 9.634	2.706 / 3.816	8.345 / 11.002	3.130 / 4.828	7.854 / 9.668	2.716 / 3.903	8.008 / 9.813	2.399 / 3.549

Table 1: Quantitative results for End-Point Error (EPE \downarrow) and Root Mean Squared Error (RMSE \downarrow) on PSSD are provided. The best-performing results in each category are highlighted in bold. Here, Δt denotes the time interval between the source and the target time.

Index	Settings		Problem 1		Problem 2		Problem 3	
	DPHT	GE	$\Delta t = 21$	$\Delta t = 11$	$\Delta t = 21$	$\Delta t = 11$	$\Delta t = 21$	$\Delta t = 11$
(A)	✓	✓	0.625	0.393	1.167	0.739	0.616	0.389
(B)	✓*	✓	0.658	0.395	1.249	0.764	0.627	0.389
(C)	✗	✓	0.757	0.403	1.278	0.777	0.630	0.391
(D)	✓	✓*	0.645	0.396	1.242	0.752	0.619	0.386
(E)	✓	✗	0.701	0.398	1.249	0.793	0.659	0.401
(F)	✗	✗	0.805	0.431	1.349	0.887	0.725	0.413

Table 2: Ablation study of our proposed modules, showing results for End-Point Error (EPE). Blocks colored greener indicate better performance, characterized by lower EPE values. ✓ indicates the presence of the module, ✗ indicates the absence, and ✓* indicates the removal of the submodules under this module, for DPHT, it refers to 3D-DPD, and for GE, it refers to GCU (including the projection and re-projection). Setting (A) represents our final model.

ing conditions.

5.3 Ablation Study

We conduct a series of ablation experiments to evaluate the contribution of each component to overall performance, as detailed in Table 2. Each column in the table is color-coded with a gradient from yellow to green, where the greener color represents better performance. These results underscore the effectiveness of the DPHT and Graph Encoder (GE) and their submodules. In Problem 1, both DPHT and GE exhibit notable improvements. In high-speed motion scenarios (Problem 2), particles in the fluid exhibit greater displacements be-

tween the source time and target time, increasing the difficulty of accurate flow prediction. Under these circumstances, the enhancements provided by the 3D-DPD submodule in DPHT and the GCU submodule in GE (7.0% and 6.4%, respectively) are the most significant across the three Problems. In Problem 3, the distinctive brightness distribution of the scene might aid feature extraction, and the improvements from DPHT and GE are comparatively less pronounced but still remain observable.

6 Conclusions

We start from the perspective of fluid (primarily turbulent) scenarios and conduct a detailed analysis of their prominent characteristics, which may pose challenges to PIV hardware and deep learning algorithms. Based on these analyses, we explore a novel approach to estimate fluid motion using spike cameras. Additionally, we develop a tailored network architecture called SIV, designed to solve PIV problems while adapting to scenario-specific features, which integrates two novel modules: DPHT and GE. DPHT is mainly used to aggregate motion features from the spike stream while retaining scene details. GE is primarily used to extract contextual features from highly unstructured turbulent scenes. We also propose a more challenging and realistic PIV dataset, PSSD, which features multiple scenarios and captures the temporal dynamics of flow field variations. Through comparative experiments, we validate that our method outperforms existing open-source PIV algorithms and spike-based optical flow algorithms on the PSSD dataset. In ablation studies, we grad-

ually remove the introduced modules and their submodules to prove their effectiveness and analyze their performance in different scenarios. In summary, this study explores the great potential of spike cameras in PIV and advocates for the use of customized network solutions for fluid motion estimation tasks.

References

- [Cai *et al.*, 2018] Shengze Cai, Etienne Mémin, Pierre Dérian, and Chao Xu. Motion estimation under location uncertainty for turbulent fluid flows. *Experiments in Fluids*, 59(1):8, 2018.
- [Cai *et al.*, 2019a] Shengze Cai, Jiaming Liang, Qi Gao, Chao Xu, and Runjie Wei. Particle image velocimetry based on a deep learning motion estimator. *IEEE Transactions on Instrumentation and Measurement*, 69(6):3538–3554, 2019.
- [Cai *et al.*, 2019b] Shengze Cai, Shichao Zhou, Chao Xu, and Qi Gao. Dense motion estimation of particle images via a convolutional neural network. *Experiments in Fluids*, 60:1–16, 2019.
- [Chen *et al.*, 2022] Bo Chen, Xiaojun Li, and Zuchao Zhu. Investigations of energy distribution and loss characterization in a centrifugal impeller through piv experiment. *Ocean Engineering*, 247:110773, 2022.
- [Chen *et al.*, 2023] Shiyan Chen, Zhaofei Yu, and Tiejun Huang. Self-supervised joint dynamic scene reconstruction and optical flow estimation for spiking camera. In *Proceedings of the AAAI Conference on Artificial Intelligence*, volume 37, pages 350–358, 2023.
- [Dong *et al.*, 2021] Siwei Dong, Tiejun Huang, and Yonghong Tian. Spike camera and its coding methods. *arXiv preprint arXiv:2104.04669*, 2021.
- [Dosovitskiy *et al.*, 2015] Alexey Dosovitskiy, Philipp Fischer, Eddy Ilg, Philip Hausser, Caner Hazirbas, Vladimir Golkov, Patrick Van Der Smagt, Daniel Cremers, and Thomas Brox. FlowNet: Learning optical flow with convolutional networks. In *Proceedings of the IEEE international conference on computer vision*, pages 2758–2766, 2015.
- [Gao *et al.*, 2021] Qi Gao, Hongtao Lin, Han Tu, Haoran Zhu, Runjie Wei, Guoping Zhang, and Xueming Shao. A robust single-pixel particle image velocimetry based on fully convolutional networks with cross-correlation embedded. *Physics of Fluids*, 33(12), 2021.
- [Han and Wang, 2023] Yuxuan Han and Qian Wang. An attention-mechanism incorporated deep recurrent optical flow network for particle image velocimetry. *Physics of Fluids*, 35(7), 2023.
- [Hu *et al.*, 2022] Liwen Hu, Rui Zhao, Ziluo Ding, Lei Ma, Boxin Shi, Ruiqin Xiong, and Tiejun Huang. Optical flow estimation for spiking camera. In *Proceedings of the IEEE/CVF Conference on Computer Vision and Pattern Recognition*, pages 17844–17853, 2022.
- [Huang *et al.*, 2017] Jing Huang, Menghan Guo, and Shoushun Chen. A dynamic vision sensor with direct logarithmic output and full-frame picture-on-demand. In *2017 IEEE International Symposium on Circuits and Systems (ISCAS)*, pages 1–4. IEEE, 2017.
- [Huang, 2019] Tiejun Huang. Method and device for encoding space-time signals, December 31 2019. US Patent 10,523,972.
- [Hui *et al.*, 2018] Tak-Wai Hui, Xiaoou Tang, and Chen Change Loy. Liteflownet: A lightweight convolutional neural network for optical flow estimation. In *Proceedings of the IEEE conference on computer vision and pattern recognition*, pages 8981–8989, 2018.
- [Ji *et al.*, 2024a] Kexin Ji, Qiang An, and Xin Hui. Cross-correlation-based convolutional neural network with velocity regularization for high-resolution velocimetry of particle images. *Physics of Fluids*, 36(7), 2024.
- [Ji *et al.*, 2024b] Kexin Ji, Xin Hui, and Qiang An. Effects of velocity regularization on neural network performance in processing particle images. *Physics of Fluids*, 36(10), 2024.
- [Kolmogorov, 1991] Andrei Nikolaevich Kolmogorov. The local structure of turbulence in incompressible viscous fluid for very large reynolds numbers. *Proceedings of the Royal Society of London. Series A: Mathematical and Physical Sciences*, 434(1890):9–13, 1991.
- [Kompenhans *et al.*, 2000] Juergen Kompenhans, Markus Raffel, Lutz Dieterle, Tim Dewhurst, Heinrich Vollmers, K Ehrenfried, Christian Willert, K Pengel, Ch Kähler, A Schröder, et al. Particle image velocimetry in aerodynamics: Technology and applications in wind tunnels. *Journal of Visualization*, 2(3-4):229–244, 2000.
- [Lagemann *et al.*, 2021] Christian Lagemann, Kai Lagemann, Sach Mukherjee, and Wolfgang Schröder. Deep recurrent optical flow learning for particle image velocimetry data. *Nature Machine Intelligence*, 3(7):641–651, 2021.
- [Lee *et al.*, 2017] Yong Lee, Hua Yang, and Zhouping Yin. Piv-dcnn: cascaded deep convolutional neural networks for particle image velocimetry. *Experiments in Fluids*, 58:1–10, 2017.
- [Li and Gupta, 2018] Yin Li and Abhinav Gupta. Beyond grids: Learning graph representations for visual recognition. *Advances in neural information processing systems*, 31, 2018.
- [Li *et al.*, 2008] Yi Li, Eric Perlman, Mingping Wan, Yunke Yang, Charles Meneveau, Randal Burns, Shiyi Chen, Alexander Szalay, and Gregory Eyink. A public turbulence database cluster and applications to study lagrangian evolution of velocity increments in turbulence. *Journal of Turbulence*, 9(N31), 2008.
- [Lichtsteiner *et al.*, 2008] Patrick Lichtsteiner, Christoph Posch, and Tobi Delbruck. A 128×128 120 db 15 μs latency asynchronous temporal contrast vision sensor. *IEEE Journal of Solid-State Circuits*, 43(2):566–576, 2008.

- [Lourenco and Krothapalli, 1995] L Lourenco and A Krothapalli. On the accuracy of velocity and vorticity measurements with piv. *Experiments in fluids*, 18(6):421–428, 1995.
- [Luo *et al.*, 2022] Ao Luo, Fan Yang, Kunming Luo, Xin Li, Haoqiang Fan, and Shuaicheng Liu. Learning optical flow with adaptive graph reasoning. In *Proceedings of the AAAI conference on artificial intelligence*, volume 36, pages 1890–1898, 2022.
- [Manickathan *et al.*, 2023] Lento Manickathan, Claudio Mucignat, and Ivan Lunati. A lightweight neural network designed for fluid velocimetry. *Experiments in Fluids*, 64(10):161, 2023.
- [MoayeriKashani *et al.*, 2016] Masoumeh MoayeriKashani, SH Lai, S Ibrahim, NMN Sulaiman, and FY Teo. Tracking the hydrodynamic behavior of fine sediment using particle image velocimetry. *Environmental Earth Sciences*, 75:1–13, 2016.
- [Moeys *et al.*, 2017] Diederik Paul Moeys, Federico Corradi, Chenghan Li, Simeon A Bamford, Luca Longinotti, Fabian F Voigt, Stewart Berry, Gemma Taverni, Fritjof Helmchen, and Tobi Delbruck. A sensitive dynamic and active pixel vision sensor for color or neural imaging applications. *IEEE transactions on biomedical circuits and systems*, 12(1):123–136, 2017.
- [Nakagawa *et al.*, 2016] Masaki Nakagawa, Stephan Kallweit, Frank Michaux, and Teppei Hojo. Typical velocity fields and vortical structures around a formula one car, based on experimental investigations using particle image velocimetry. *SAE International Journal of Passenger Cars-Mechanical Systems*, 9(2016-01-1611):754–771, 2016.
- [Nobach and Honkanen, 2005] H Nobach and M Honkanen. Two-dimensional gaussian regression for sub-pixel displacement estimation in particle image velocimetry or particle position estimation in particle tracking velocimetry. *Experiments in fluids*, 38:511–515, 2005.
- [Posch *et al.*, 2010] Christoph Posch, Daniel Matolin, and Rainer Wohlgenannt. A qvga 143 db dynamic range frame-free pwm image sensor with lossless pixel-level video compression and time-domain cds. *IEEE Journal of Solid-State Circuits*, 46(1):259–275, 2010.
- [Raschi *et al.*, 2012] Marcelo Raschi, Fernando Mut, Greg Byrne, Christopher M Putman, Satoshi Tateshima, Fernando Viñuela, Tetsuya Tanoue, Kazuo Tanishita, and Juan R Cebal. Cfd and piv analysis of hemodynamics in a growing intracranial aneurysm. *International journal for numerical methods in biomedical engineering*, 28(2):214–228, 2012.
- [Rebecq *et al.*, 2019] Henri Rebecq, René Ranftl, Vladlen Koltun, and Davide Scaramuzza. High speed and high dynamic range video with an event camera. *IEEE transactions on pattern analysis and machine intelligence*, 43(6):1964–1980, 2019.
- [Selvan *et al.*, 2020] Raghavendra Selvan, Thomas Kipf, Max Welling, Antonio Garcia-Uceda Juarez, Jesper H Pedersen, Jens Petersen, and Marleen de Bruijne. Graph refinement based airway extraction using mean-field networks and graph neural networks. *Medical image analysis*, 64:101751, 2020.
- [Sun *et al.*, 2018] Deqing Sun, Xiaodong Yang, Ming-Yu Liu, and Jan Kautz. Pwc-net: Cnns for optical flow using pyramid, warping, and cost volume. In *Proceedings of the IEEE conference on computer vision and pattern recognition*, pages 8934–8943, 2018.
- [Teed and Deng, 2020] Zachary Teed and Jia Deng. Raft: Recurrent all-pairs field transforms for optical flow. In *Computer Vision—ECCV 2020: 16th European Conference, Glasgow, UK, August 23–28, 2020, Proceedings, Part II 16*, pages 402–419. Springer, 2020.
- [Willert and Klinner, 2022] Christian E Willert and Joachim Klinner. Event-based imaging velocimetry: an assessment of event-based cameras for the measurement of fluid flows. *Experiments in Fluids*, 63(6):101, 2022.
- [Willert, 2023] Christian E Willert. Event-based imaging velocimetry using pulsed illumination. *Experiments in Fluids*, 64(5):98, 2023.
- [Xia *et al.*, 2024] Lujie Xia, Ziluo Ding, Rui Zhao, Jiyuan Zhang, Lei Ma, Zhaofei Yu, Tiejun Huang, and Ruiqin Xiong. Unsupervised optical flow estimation with dynamic timing representation for spike camera. *Advances in Neural Information Processing Systems*, 36, 2024.
- [Yu *et al.*, 2021] Changdong Yu, Xiaojun Bi, Yiwei Fan, Yang Han, and Yunfei Kuai. Lightpivnet: An effective convolutional neural network for particle image velocimetry. *IEEE Transactions on Instrumentation and Measurement*, 70:1–15, 2021.
- [Zhang and Piggott, 2020] Mingrui Zhang and Matthew D Piggott. Unsupervised learning of particle image velocimetry. In *High Performance Computing: ISC High Performance 2020 International Workshops, Frankfurt, Germany, June 21–25, 2020, Revised Selected Papers 35*, pages 102–115. Springer, 2020.
- [Zhang *et al.*, 2023a] Wei Zhang, Xue Dong, Zhiwei Sun, and Shuogui Xu. An unsupervised deep learning model for dense velocity field reconstruction in particle image velocimetry (piv) measurements. *Physics of Fluids*, 35(7), 2023.
- [Zhang *et al.*, 2023b] Wei Zhang, Xiangyu Nie, Xue Dong, and Zhiwei Sun. Pyramidal deep-learning network for dense velocity field reconstruction in particle image velocimetry. *Experiments in Fluids*, 64(1):12, 2023.
- [Zhao *et al.*, 2022] Rui Zhao, Ruiqin Xiong, Jing Zhao, Zhaofei Yu, Xiaopeng Fan, and Tiejun Huang. Learning optical flow from continuous spike streams. *Advances in Neural Information Processing Systems*, 35:7905–7920, 2022.
- [Zhao *et al.*, 2024] Rui Zhao, Ruiqin Xiong, Jian Zhang, Xinfeng Zhang, Zhaofei Yu, and Tiejun Huang. Optical flow for spike camera with hierarchical spatial-temporal spike fusion. In *Proceedings of the AAAI Conference on Artificial Intelligence*, pages 7496–7504, 2024.

[Zheng *et al.*, 2022] Zihua Zheng, Ni Nie, Zhi Ling, Pengfei Xiong, Jiangyu Liu, Hao Wang, and Jankun Li. Dip: Deep inverse patchmatch for high-resolution optical flow. In *Proceedings of the IEEE/CVF Conference on Computer Vision and Pattern Recognition*, pages 8925–8934, 2022.

Spike Imaging Velocimetry: Dense Motion Estimation of Fluids Using Spike Cameras

Anonymous submission

1 This supplementary material provides important details
2 that are not fully covered in the main text of submission
3 355, including a comprehensive introduction to the Parti-
4 cle Scenes with Spike and Displacement Data Generation
5 (PSSD) dataset, details of our proposed method, and test re-
6 sults on real-world data. We have included the code imple-
7 mentation of our proposed SIV in the appendix. The pre-
8 trained models and some test data can be downloaded from
9 the anonymous link [https://anonymous.4open.science/r/SIV-](https://anonymous.4open.science/r/SIV-8102/)
10 8102/.

11 1 Particle Scenes with Spike and 12 Displacement

13 1.1 Data Generation

14 Constructing the Particle Scenes with Spike and Displace-
15 ment (PSSD) dataset involves three steps: position simula-
16 tion, scene generation, and spike simulation.

17 **Position Simulation.** As an initialization step, we ran-
18 domly generate the coordinates of $N = \rho \times H_{box} \times W_{box}$
19 particles within a plane of dimensions $H_{box} \times W_{box}$. We then
20 calculate and record the coordinate changes of all particles
21 frame by frame under the influence of the steady flow ΔD
22 obtained from JHTDB [?]:

$$\begin{cases} x_{t+1} = x_t + \Delta D_{x,t}(x_t, y_t) \\ y_{t+1} = y_t + \Delta D_{y,t}(x_t, y_t) \end{cases} \quad (1)$$

23 For each pixel, we calculate the total displacement D within
24 the time interval from t_0 to t_1 of the predicted displacement
25 field as the ground truth:

$$\begin{cases} D_x(x_0, y_0) = \sum_{t=t_0}^{t=t_1} \Delta D_{x,t}(x_t, y_t) \\ D_y(x_0, y_0) = \sum_{t=t_0}^{t=t_1} \Delta D_{y,t}(x_t, y_t) \end{cases} \quad (2)$$

26 We determine different average displacements based on dif-
27 ferent problems and time intervals dt (see Section 1.3)

28 **Scene Generation.** For each time t , we use particles lo-
29 cated within the range $\{(x, y) | 30 \leq x < 286, 30 \leq y < 286\}$
30 to generate the scene. Specifically, considering diffraction
31 around the central coordinates based on the particle diam-
32 eter d_p , the brightness of particles I follows a Gaussian

formula[?]:

$$I(x, y) = I_0 \cdot \exp\left[\frac{-(x - x_0)^2 - (y - y_0)^2}{(1/8)d_p^2}\right] \quad (3)$$

34 If multiple particles overlap during motion, previous
35 datasets[?] typically handle this with simple digital overflow
36 treatment. Here, we strictly sum the brightness in the over-
37 lapping regions:

$$I(x, y) = \sum_{i=0}^{i=q} I_i(x, y), \quad (4)$$

38 where q is the number of overlapping particles at that posi-
39 tion.

40 **Spike simulation.** Unlike conventional cameras that syn-
41 chronize all sensors with a fixed exposure time, spike cameras
42 continuously capture photons, generating a spike when the
43 light intensity exceeds a predefined threshold. This unique
44 operating mechanism is known as "Integral-and-Fire" (IF),
45 and cameras designed based on this concept are referred to as
46 spike cameras. Because they don't require synchronized ex-
47 posure, spike cameras can achieve a high dynamic range on
48 each pixel. Each sensor creates a time-ordered sequence of
49 visual elements in a spike camera, where the simplest form
50 is a bitstream. A '1' indicates that a spike has occurred at
51 that moment, while a '0' means the sensor is in an accumula-
52 tion state. The sequence of zeros between consecutive spikes
53 forms a digital visual element. Each sensor generates a spike
54 stream, and the collection of all spike streams from every sen-
55 sor forms an array of spike streams. The IF mechanism can
56 be mathematically represented as follows:

$$A(\mathbf{x}, t) = \int_0^t \alpha \cdot I(\mathbf{x}, \tau) \bmod \theta, \quad (5)$$

57 where $A(\mathbf{x}, t)$ is the voltage of the accumulator at pixel $\mathbf{x} =$
58 (x, y) at time τ . θ is the threshold of the comparator. The
59 output of the spike camera is a spatio-temporal binary stream
60 S of size $H \times W \times N$, where H and W are the height and
61 width of the sensor, respectively, and N is the time step of
62 the spike stream. Compared to traditional cameras, the spike
63 camera retains richer visual information in terms of time and
64 brightness representation. Following the approach outlined
65 in related spike camera work[?; ?; ?; ?; ?], we simulate the

66 Integral-and-Fire (IF) mechanism by setting the threshold θ to
 67 1024 and the number of time steps N to 62. To add realism,
 68 we introduce Gaussian noise with mean $\mu = 0$ and standard
 69 deviation $\sigma = 15$. This simulation process provides a spike
 70 sequence that mimics the output of a spike camera.

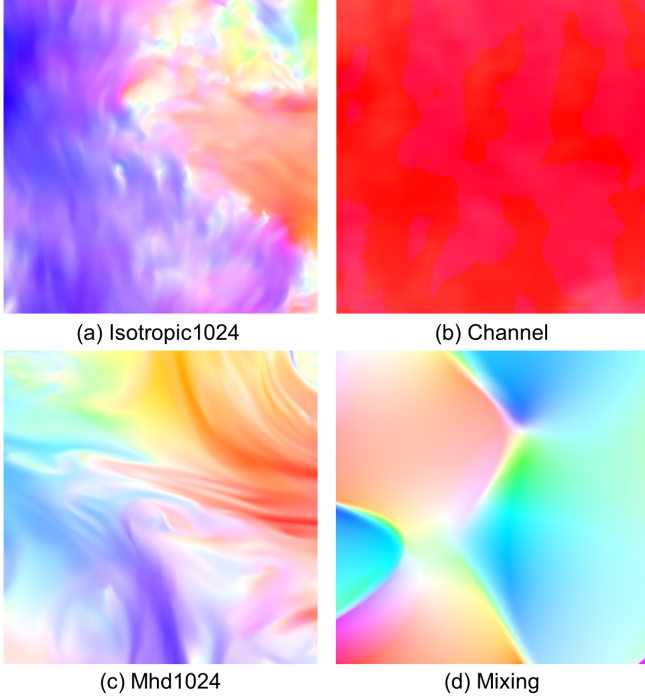


Figure 1: Visualizations of the four types of flow fields: (a) Isotropic1024, (b) Channel (c) Mhd1024, and (d) Mixing.

71 1.2 Scene Details

72 The dataset consists of simple scenarios (Problem 1), large
 73 displacement scenarios (Problem 2), and high dynamic range
 74 scenarios (Problem 3). For Problem 1 and Problem 2, we
 75 follow the scene design scheme from previous work[?; ?;
 76 ?], including particle density, particle diameter, and particle
 center brightness, as detailed in Table 1. We assume that in

Table 1: Parameters for particle scenes initialization for Problem 1 and Problem 2.

Parameter	Range	Unit
Seeding density ρ	0.05-0.1	Particle per pixel
Particle diameter d_p	2-4	Pixel
Location (x_0, y_0)	0-255	Pixel
Peak intensity I_0	200-255	Grey value

77 both Problem 1 and Problem 2, the scene’s brightness varia-
 78 tion generally does not exceed the dynamic range of conven-
 79 tional high-speed cameras. Additionally, we disregard any
 80 relationship between brightness and particle coordinates, as-
 81 suming that changes in particle position do not affect parti-
 82 cle brightness. Regarding brightness overflow due to particle
 83

overlap, previous datasets[?] simply allowed uint8 data over-
 flow in those regions. We consider this to be unreasonable,
 so we truncate the pixel values at that position to 255. It’s
 worth noting that this cap applies to both image and spike
 stream generation, which objectively limits the performance
 of spike camera algorithms because it reduces the original dy-
 namic range of the spike stream data, thereby diminishing the
 contrast between different brightness regions.

For Problem 3, we consider scenarios with greater bright-
 ness differences and instances where particle position move-
 ment is partially coupled with brightness changes. These con-
 siderations are based on two aspects observed in experimen-
 tal PIV scenarios: (1) The clustering and dispersion of parti-
 cles during motion can lead to variations in regional bright-
 ness. (2) Different types of tracer particles (such as fluo-
 rescent particles, metal-coated spheres, or hollow glass beads)
 have varying surface characteristics, with some opaque parti-
 cles capable of generating stronger signals. This implies that
 they exhibit significant light scattering. Since illumination
 in experiments typically comes from a single direction, light
 scattering from the particles and the fluid causes the signal
 to diminish as the light penetrates deeper into the fluid. This
 effect can vary depending on fluid type and the type of tracer
 particles used, among other factors. In addition to the two
 aforementioned factors, other specific scenarios—such as ex-
 treme lighting conditions or the introduction of obstacles in
 the flow field—could lead to brightness distributions that ex-
 ceed the dynamic range of experimental high-speed cameras,
 resulting in overexposed or underexposed areas within the
 images. Thus, we designed Problem 3 to investigate these
 situations. Besides brightness distribution, the settings for
 Problem 3 are generally consistent with those for Problems
 1 and 2. However, to increase the frequency of particle over-
 lap, Problem 3 uses relatively larger particle diameters. The
 parameter settings are shown in Table 2. We assume that the

Table 2: Parameters for particle scenes initialization for Problem 3.

Parameter	Range	Unit
Seeding density ρ	0.05-0.1	Particle per pixel
Particle diameter d_p	3-4	Pixel
Location (x_0, y_0)	0-255	Pixel

lighting is oriented along the y-axis. The central brightness
 of the particles decreases as y increases, following this atten-
 uation pattern:

$$I_0 = 511 \cdot \exp(-0.00546y) \quad (6)$$

A spike camera can record the brightness in this scenario with
 fine granularity, which conventional high-speed cameras can-
 not. Assuming that the latter has a dynamic range of 0-255,
 the actual brightness variations would already exceed this
 range. To address this, we adjust the overall dynamic range
 of conventional high-speed cameras to ensure it encompass
 most of the scene’s brightness variation. However, even with
 this adjustment, some regions in the image may still appear
 overly bright or too dark. The visualization of the scene is
 shown in Figure 2.

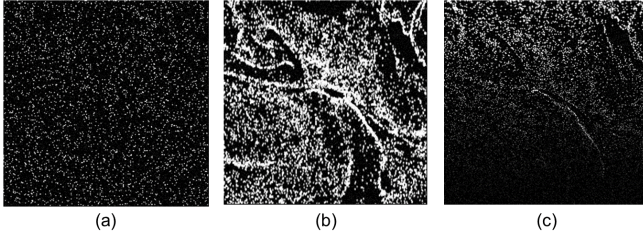


Figure 2: Example scenes of PSSD. Problem 2 exhibits more significant displacements compared to Problem 1, while Problem 3 shows distinct variations in brightness.

1.3 Displacement Statistics

We introduce four types of flow fields from JHTDB[?]
—Isotropic1024, Channel, Mhd1024, and Mixing—
as the actual movements that occur among the particles
in our scenarios (as shown in Figure 1).

For Problem 1, Problem 2, and Problem 3 in the PSSD
dataset, the number of samples in the training and test sets
is shown in Table 3.

Table 3: The number of samples in the training and test sets for Problem 1, 2, and 3.

Flow field	Training set	Test set
Isotropic1024	2500	1000
Channel	2500	1000
Mhd1024	2500	1000
Mixing	2500	1000
Total	10000	4000

The distribution of pixel displacements for all samples in
Problem 1, Problem 2, and Problem 3 is shown in Figures 3,
4, and 5, respectively.

2 Details of Our Method

2.1 Overall Architecture

Problem definition. Let $\mathbf{S} \in \mathbb{B}^{H \times W \times T}$ represent the spike
stream recorded by the spike camera. \mathbb{B} is the binary domain.
We aim to estimate the displacement \mathbf{D} of particles in the
fluid between time moments t and $t + \Delta t$. At the pixel level,
for any given pixel $\mathbf{p} = (x, y)$ at t , we need to find a unique
correspondence formulated by:

$$\mathcal{I}(\mathbf{p}, t) \leftarrow \mathcal{I}(\mathbf{p}, t + \Delta t). \quad (7)$$

Here, \mathcal{I} is the mapping of the spike stream \mathbf{S} in the high-
dimensional feature space, representing the scene information,
i.e., $\mathcal{I} = \text{Rep}(\mathbf{S})$.

Network architecture. The structure of the SIV network is
shown in Figure 6. To represent the scenes at moments t
and $t + \Delta t$, we extract spike stream segments (source and
target) near these two moments, denoted as \mathbf{S}_s and \mathbf{S}_t , and
input them into the network. Firstly, through the proposed
DPHT module, the sub-stream \mathbf{S}_s and \mathbf{S}_t are embedded into
the representations \mathbf{R}_s and \mathbf{R}_t by our proposed DPHT module.
Motion features $\mathbf{F}_{s,m}$ and $\mathbf{F}_{t,m}$ are extracted from \mathbf{R}_s

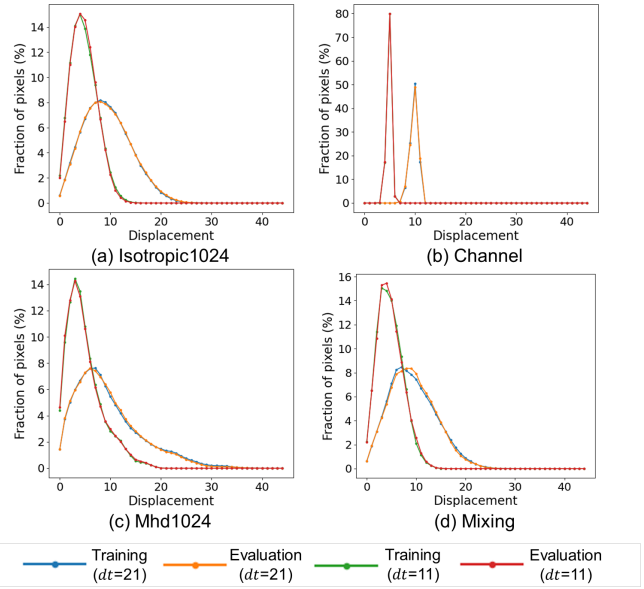


Figure 3: The distribution of pixel displacements for all samples of 4 types of flow field in Problem 1. The unit of displacement is pixel.

and \mathbf{R}_t . Through the proposed Graph Encoder, the context
feature \mathbf{F}_c is extracted from \mathbf{R}_t . Subsequently, the enhanced
features $\mathbf{F}_{s,m}$, $\mathbf{F}_{t,m}$ and \mathbf{F}_c undergo an iterative optimization
process in a pyramid structure, ranging from coarse (1/16
downsampled branch) to fine (1/4 downsampled branch). In
each branch, similar to DIP[?], the Inverse Patchmatch Block
is used to construct the correlation volume, and is aggregated
through a GRU. Finally, the Local Search Block estimates
the residual displacement field $\Delta \mathbf{D}$ by searching for local
cost based on the current displacement field estimate, and
cost aggregation is performed through another GRU. To facilitate
batch operations in deep learning networks and reduce
computational costs, the Multi-scale Iterative Optimizer
introduces the inverse PatchMatch module[?] in step 1. This
module primarily consists of inverse propagation and local
search blocks. Inverse propagation can be summarized by the
following equation:

$$\text{Corr}^\lambda = F_1^\lambda \cdot \mathbf{W}(\mathbf{S}(F_2^\lambda, \Delta p), \text{flow}_0^\lambda), \quad (8)$$

where λ represents the downsampling factor, which is 1/4 or
1/16 in this paper, $\mathbf{S}(F_2, \Delta p)$ represents translating F_2 by a
small distance Δp , and $\mathbf{W}(\cdot)$ represents warping the shifted
feature map based on the initial optical flow. This equation
holds because the movement of optical flow essentially corresponds
to the reverse of the feature map movement, with Δp
being relatively small compared to warping [?]. In the second
step, a GRU network is used to perform the first update

$$\Delta \text{flow}_1^\lambda = \text{GRU}_1(\text{flow}_0^\lambda, \text{Corr}^\lambda, F_c^\lambda), \quad (9)$$

where Δflow_1 represents the residual optical flow predicted
by GRU_1 . Therefore, the updated optical flow is denoted as
 $\text{flow}_1^\lambda = \text{flow}_0^\lambda + \Delta \text{flow}_1^\lambda$. The third stage is local search.
Given an optical flow increment Δf where the updated correlation
is represented as

$$\text{Corr}_{LS}^\lambda = F_1^\lambda \cdot \mathbf{S}(\mathbf{W}(F_2^\lambda), \Delta f), \quad (10)$$

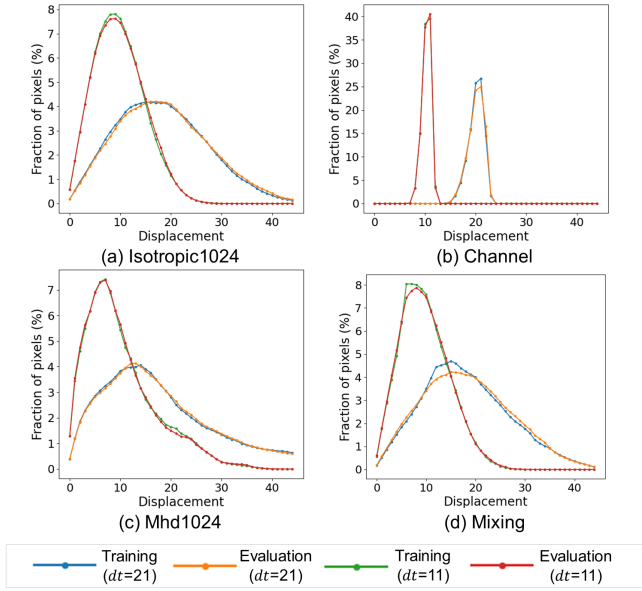


Figure 4: The distribution of pixel displacements for all samples of 4 types of flow field in Problem 2. The unit of displacement is pixel.

where $Corr_{LS}$ represents the correlation updated from local search. Finally, iterative refinement is performed by the second GRU to obtain the residual optical flow

$$\Delta flow_2^\lambda = GRU_2(flow_1^\lambda, Corr_{LS}^\lambda, F_c^\lambda), \quad (11)$$

and the updated optical flow can be expressed as $flow_2^\lambda = flow_1^\lambda + \Delta flow_2^\lambda$.

2.2 Detail-Preserving Hierarchical Transform

[?] demonstrates that using a multi-layer hierarchical structure to characterize spike streams can effectively suppress the influence of randomness in spikes and enhance the feature extraction capability of the network. Low-level features mainly focus on local details, while high-level features aggregate these low-level features to express more complex meanings. However, our ablation experiments show that directly using multi-level representations does not achieve optimal performance improvement for PIV. This is because, as mentioned in the Introduction, the reduction in resolution or scale of feature maps leads to a significant loss of detail information. Furthermore, these details may not be critical for macroscopic objects, but considering that the particles in PIV are small and the fluid motion is highly intricate and complex, even the loss of detail information could result in an increase in local prediction errors. Moreover, the sparse and dark regions without particles essentially carry little to no signal, much of the information in a small region may stem from the bright particles. Based on these considerations, we designed a 3D Detail-Preserving Downsampling unit in which a bunch of 3D convolutions and 3D max poolings are incorporated (as shown in Figure 7(a)) to reduce the progressive loss of important information across the multi-layer structure while enabling the network to aggregate features at multiple scales. We refer to the entire block in Figure 7(a) as the Detail-Preserving Hierarchical Transform (DPHT).

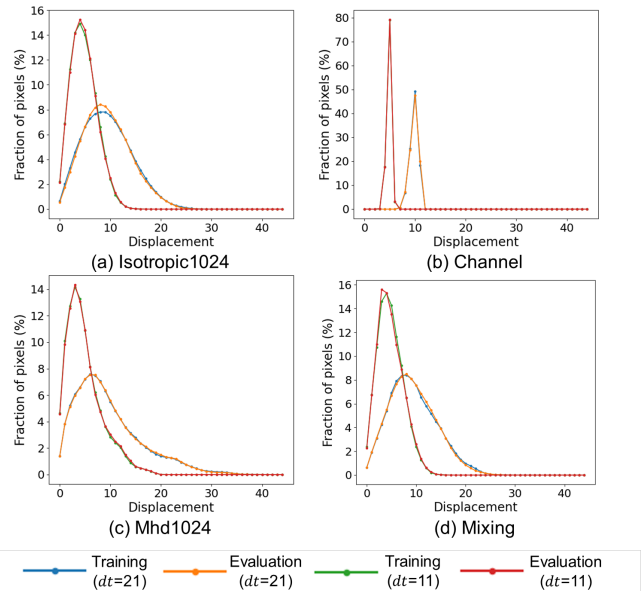


Figure 5: The distribution of pixel displacements for all samples of 4 types of flow field in Problem 3. The unit of displacement is pixel.

3D Detail-Preserving downsampling. As shown in Figure 7(a), suppose the input of level l is a feature vector $\mathbf{x}^{(l)}$, and the processing of $\mathbf{x}^{(l)}$ at this level is as follows:

$$\mathbf{x}_{out}^{(l)} = \mathcal{D}^{(l)}(\mathbf{x}^{(l)}) = \mathcal{F}_{2C}(\mathcal{F}_{3C}(\mathbf{x}^{(l)}) + \mathcal{F}_{3MP}(\mathbf{x}^{(l)})), \quad (12)$$

Here, \mathcal{F}_{3C} represents a $5 \times 3 \times 3$ 3D convolution, \mathcal{F}_{3MP} is a combination of a 3D max pooling operation and a $5 \times 1 \times 1$ 3D convolution, and \mathcal{F}_{2C} refers to a sequential stack of 2D convolutions. The output of the previous level serves as the input to the next level, i.e., $\mathbf{x}^{(l+1)} = \mathbf{x}_{out}^{(l)} = \mathcal{D}^{(l)}(\mathbf{x}^{(l)})$.

Global temporal aggregation. In this step, the output feature vectors from each level are further refined by several convolutions (for detailed information, refer to the supplementary materials), and then concatenated together to form the final representation of the DPHT:

$$\mathbf{R} = \mathcal{A}_m[\mathbf{x}_{out}^{(l=1)} \oplus \mathbf{x}_{out}^{(l=2)} \oplus \mathbf{x}_{out}^{(l=3)}], \quad (13)$$

\oplus represents concatenation, and \mathcal{A}_m denotes convolution. As shown in Figure 7, we use DPHT as a pre-representation method before motion feature extraction and context information extraction, obtaining \mathbf{R}_s and \mathbf{R}_t for source sub-stream and target sub-stream, respectively.

2.3 Graph Encoder

Turbulent motion is highly complex, and extracting context information from turbulence is challenging. Therefore, [?] argued that context extractors are unnecessary for PIV and removed this structure from their network. However, we hold a different view: despite the spatially chaotic nature of turbulence, there still exist multi-scale vortex structures (referred to as quasi-order structures), making the extraction of context information meaningful. To achieve this, we introduce Graph Convolutional Unit (GCU) in the context extractor, referring

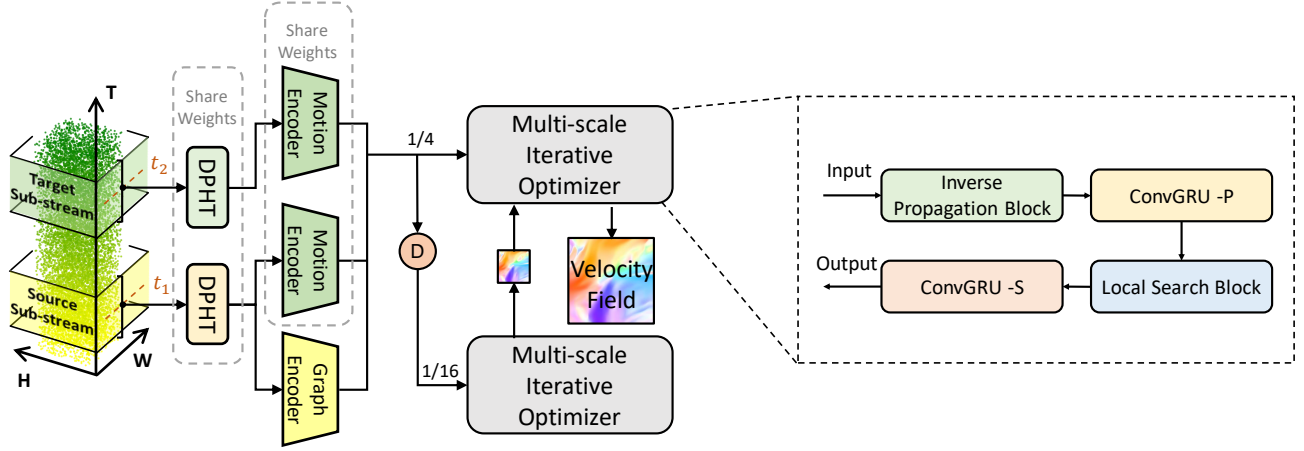


Figure 6: The overall network architecture of SIV.

252 to the entire context extractor as the Graph Encoder. Graph
 253 convolutions weight the relationships between nodes using an
 254 adjacency matrix, performing local aggregation. Each node
 255 not only focuses on its own features but also passes infor-
 256 mation from neighboring nodes (as defined by the adjacency
 257 matrix) to itself. We believe that this approach is particu-
 258 larly suited for capturing spatial or topological structures in
 259 the PIV data, especially when the quasi-order structures of
 260 the flow is highly complex topologically. This situation arises
 261 particularly in cases with extremely high flow speeds (mean-
 262 ing high Reynolds numbers). When the Reynolds number
 263 is sufficiently high, turbulence experiences a cascade process
 264 from large-scale vortices to small-scale vortices (Kolmogorov
 265 scale) [?]. This cascade process is the transfer of energy from
 266 large vortices to small vortices in turbulence, with each vor-
 267 tex disturbing the surrounding flow field, further complicating
 268 the flow.

269 **Graph projection.** The first step is to map the preliminary
 270 context information $\mathbf{R}_c = \mathbf{R}_s$ extracted from DPHT from the
 271 general coordinate space to the graph space. The projec-
 272 tion operation decouples the position information from the
 273 original grid features, making the resulting low-dimensional
 274 node feature representations more compact and expressive.
 275 The mapped context node representations, denoted as $\mathbf{V}_c =$
 276 $\{v_c^1, \dots, v_c^n\}$, contain appearance features related to the
 277 shape and regional information of the scene context. Given
 278 \mathbf{R}_c , we can use the projection function $\mathcal{P}_{R \rightarrow V}(\cdot)$ to assign
 279 features with similar representations to the same node, result-
 280 ing $\mathbf{V}_c \in \mathbb{R}^{C \times K}$, where C indicates channel number and K
 281 is a hyper-parameter representing the number of nodes. Since
 282 $\mathcal{P}_{R \rightarrow V}(\cdot)$ we define is a linear combination of feature vectors
 283 within the grid space, i.e., $\mathbf{V}_c = \mathcal{P}_{R \rightarrow V}(\mathbf{R}_c)$, the resulting
 284 nodes can theoretically aggregate both long-range and short-
 285 range information across the entire feature map, which could
 286 be beneficial for turbulent scenes with multi-scale quasi-order
 287 structures. This is formulated by,

$$v_{c,i} = \mathcal{N}\left(\sum_{\forall j} z_{ij} \cdot \mathbf{R}_{c,j}\right). \quad (14)$$

288 Here, $\mathcal{N}(\cdot)$ is the L_2 -normalization function applied to

289 the channel dimension of each node vector, and z_{ij} de-
 290 notes the projection weights computed by a CNN, i.e., $z =$
 291 $\mathcal{F}_{R \rightarrow V}(\mathbf{R}_c) \in \mathbb{R}^{(H \times W) \times K}$.

292 **Graph convolution.** After obtaining the nodes \mathbf{v}_c in the
 293 graph space, the adjacency matrix $\mathbf{A} = \mathbf{V}_c^T \mathbf{V}_c$ can be de-
 294 rived by calculating the similarity between all node vectors.
 295 We utilize the graph convolution \mathcal{G} from [?] to further prop-
 296 agate information across the graph. Specifically, for a single
 297 graph convolution with its parameter W_g , the operation is de-
 298 fined as

$$\mathbf{V}'_c = \mathcal{G}(\mathbf{V}_c, \mathbf{A}) = \sigma(\mathbf{A} \mathbf{V}_c^T W_g), \quad (15)$$

299 where $\sigma(\cdot)$ is a non-linear activation function. Two serial
 300 graph convolutional networks (GCNs) are used to capture the
 301 relationships between nodes. The node features updated by
 302 the GCNs are given by

$$\mathbf{V}_c^{\text{out}} = \mathcal{G}_2[\mathcal{G}_1(\mathbf{V}_c, \mathbf{A}), \mathbf{A}], \quad (16)$$

303 **Graph re-projection.** Our graph re-projection operation
 304 $\mathcal{P}_{V \rightarrow R}(\cdot)$ takes the transformed vertex features $\mathbf{V}_c^{\text{out}}$ and
 305 the projection weight matrix $\mathbf{Z} = [z_{ij}]$ as inputs, generat-
 306 ing a 2D feature map $\tilde{\mathbf{R}}_c$. Since inverting the projection
 307 weight matrix is not feasible, we follow the approach in [?;
 308 ?] and compute the enhanced grid context features $\tilde{\mathbf{R}}_c$ by re-
 309 weighting the vertex features $\mathbf{V}_c^{\text{out}}$. This is given by,

$$\tilde{\mathbf{R}}_c = \mathcal{P}_{V \rightarrow R}(\mathbf{V}_c^{\text{out}}, \mathbf{Z}) = \mathbf{Z} \mathbf{V}_c^{\text{out}T}. \quad (17)$$

310 Thus, $\mathcal{P}_{V \rightarrow R}$ thus linearly interpolates 2D pixel features
 311 based on the node assignments of the 2D grid features, with-
 312 out additional parameters. Note that even if two pixels are
 313 assigned to the same node, they will have different features
 314 after re-projection. Therefore, the GCU may preserve the spa-
 315 tial details of the signal. Finally, these projection results can
 316 be integrated into an existing residual extractor network \mathcal{R}
 317 introduced by [?]. Final context feature \mathbf{F}_c given by,

$$\mathbf{F}_c = \mathcal{R}(\mathbf{R}_c + \alpha \tilde{\mathbf{R}}_c), \quad (18)$$

318 where α denotes a learnable parameter that is initialized as 0
 319 and gradually performs a weighted sum.

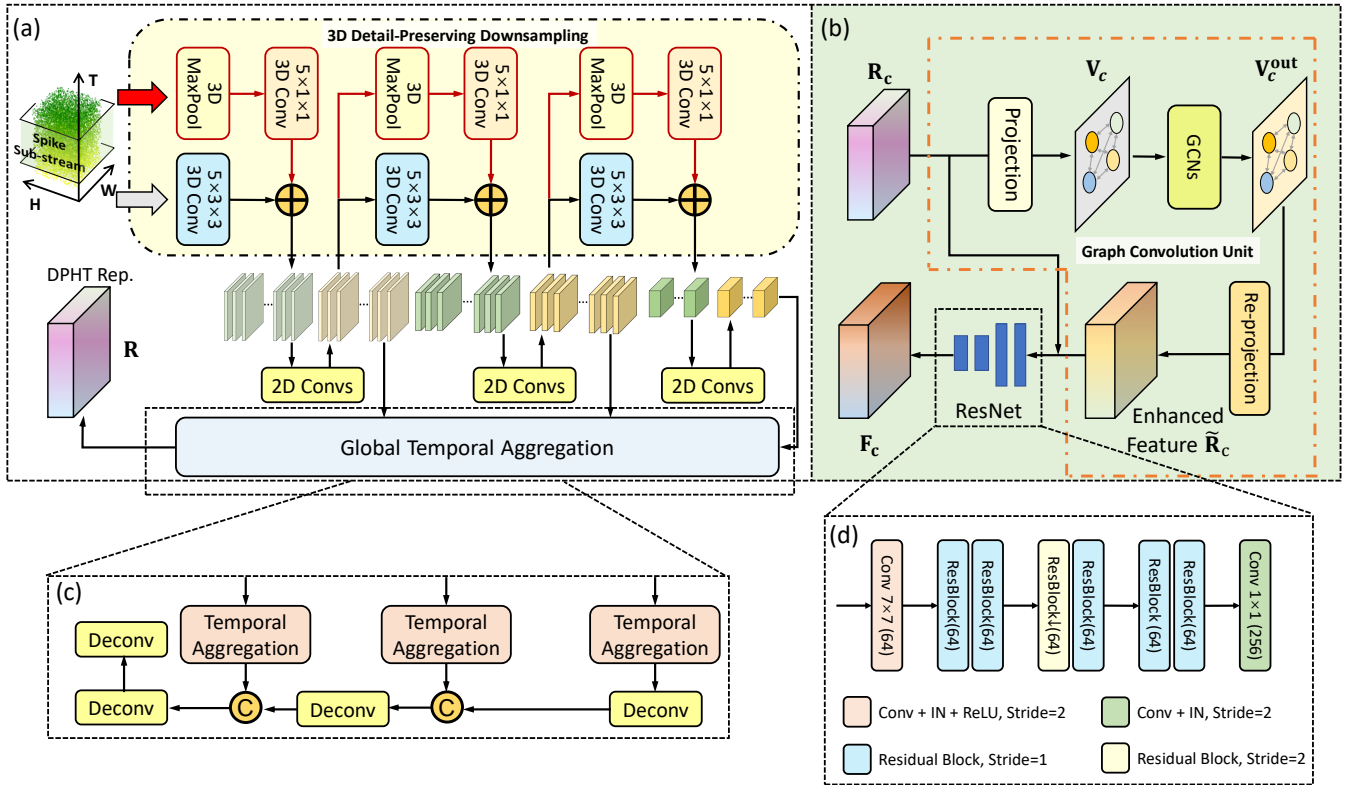


Figure 7: (a) A demonstration of the Detail-Preserving Hierarchical Transform (DPHT) structure. (b) A brief illustration of Graph Encoder (GE) structure. (c) A schematic of Global Temporal Aggregation. (d) A detailed schematic of the ResNet feature extraction module in the Graph Encoder. This structure is the same as the Motion Encoder.

320 3 Visualized Results on Real Data

321 We use a spike camera with a resolution of 400×250 to capture
 322 the process of a paramecium feeding on tiny particles.
 323 This scene is quite complex and involves a sparse distribu-
 324 tion of tracer particles. In this setup, the small particles move
 325 with the swinging motion of the paramecium’s cilia. We calcu-
 326 late the standard deviation of the spike stream-based recon-
 327 structed video over time to approximate the trajectory of the
 328 particle movement, as illustrated in Figure 8(c). We use SIV
 329 to predict the motion of particles at a certain moment, which
 330 generally aligns with the tangent direction of the trajectory.
 331 It should be noted that, due to the sparser distribution of par-
 332 ticles in this scenario and the continuous disturbance of the
 333 flow field by the paramecium, there may be errors in the esti-
 334 mation of the displacement field in vacant regions. This exam-
 335 ple primarily serves to validate the feasibility of real-shot
 336 data for our trained network model.

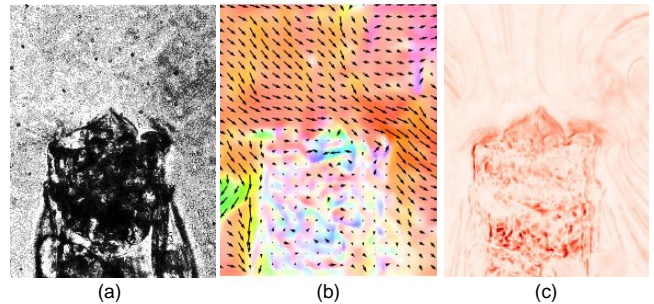


Figure 8: Visualization of the Predicted Displacement Field in Real Scenes. (a) Reconstructed image of paramecium from spike streams. (b) The instantaneous flow field of paramecium predicted by SIV trained on Problem 3. (c) The temporal standard deviation of the reconstructed image sequence, used to roughly illustrate the motion trajectories of particles and paramecium in the scene.